Model Validation for Scanning Electron Microscopy

O.Yu. Ridzel, W. Yamane, I. Mansaray, and J.S. Villarrubia[†]
National Institute of Standards and Technology, Gaithersburg, MD 20899

ABSTRACT

We are beginning projects to validate the physics models used for interpretation of electron microscopy images. In one of them, we will measure electron yields and energy spectra from cleaned well-characterized samples subjected to electron bombardment inside of a spherical retarding field analyzer in ultra-high vacuum. In another, we will measure the same features, lithographically patterned on free-standing Si membranes, with measurement techniques that differ in their interaction physics. A modeling project will compare measurement results with simulations using existing and new models. Good models should predict the observed yields and produce agreement among measurement techniques.

Keywords: critical dimension, electron microscopy, electron transport modeling, nanometer-scale dimensional metrology, secondary electron yield measurement, SEM, STEM

1. INTRODUCTION

By 2025, it is expected that transistors will be manufactured with features approaching 5 nm and require measurement uncertainties of no more than 0.31 nm.[1] Good models of the instrument/sample interaction physics are required to quantitatively interpret measurements with such uncertainties. Compared to backscattered electrons, emitted secondary electrons (SE) have lower energy so can be more efficiently gathered by electric fields and detected, are more numerous at beam energies below a few kilo-electron-volts, and are more sensitive to surface topography. They are for this reason the more important signal electrons in SEM metrology. However, SE are most numerously generated with initial energy close to the plasmon energy, around 15 eV to 25 eV for most materials. Uncertainty in the correct low-energy physics[2] leaves room for different models.

The models under consideration agree well at incident electron energies greater than a few hundred electron-volts, but they diverge at low energy with, e.g., a spread of more than a factor of two in calculated inelastic mean free paths (IMFPs) in water at 20 eV.[3] The spread in calculated SE yields (ratio of emitted SE to incident beam electrons) is similar. In such cases, one ordinarily relies on measurements to determine an appropriate model, but the corresponding measurements also disagree, often by factors of 2 or more. In copper, for example, maximum SE yields vary by about a factor of 1.8 for data collected in Joy's database.[4] Even in a more closely curated subset of these, variation is about 35 % (Fig. 1). These discrepancies limit the usefulness of the data for distinguishing good from bad models.

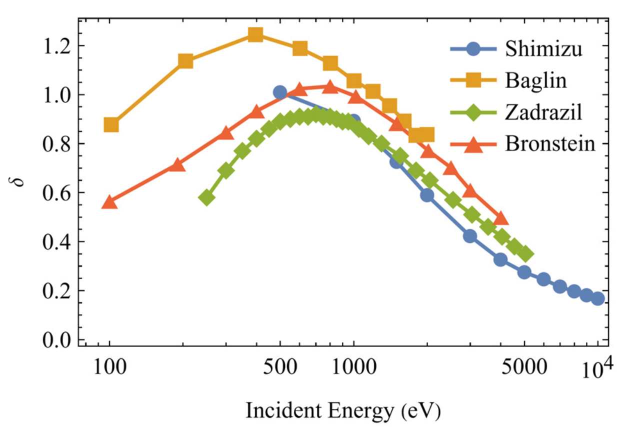

Figure 1. Comparison of experimental SE yield, δ, for Cu from Shimizu,[5] Baglin,[6] Zadražil,[7] and Bronstein.[8] The database for these did not provide uncertainties, but curves are smooth relative to curve-to-curve differences, suggesting errors are mainly systematic.

We are therefore beginning a cluster of projects aimed at model validation and improvement. Two of the projects are aimed at obtaining data suitable for testing and winnowing models. These are a yield metrology project and a measurement intercomparison project. They seek to measure quantities predicted by the models. The final project is a theoretical one. It is aimed at model improvement in response to and in anticipation of model/measurement discrepancies uncovered by the first two. In this conference report, we will describe these promising projects in Sections 2 through 4

†. John.Villarrubia@nist.gov

respectively. The projects started recently. The first is still under construction. For the others, we will present at most some preliminary measurements or calculation results.

2. YIELD METROLOGY

Emitted SE are conventionally defined operationally as those that emerge from the sample with less than 50 eV. Higher energy electrons are considered to be beam electrons that are backscattered (or transmitted if the sample is thin). A typical instrument for SE yield studies is based on the retarding field method and consists in simplest form of a hemispherical capacitor or collector with hemispherical grids placed between the sample and the collector.[9] An electron source is placed above the sample allowing the electron beam to perpendicularly hit the sample surface. Applying a retarding bias to the grid makes it a high pass energy filter, i.e., a retarding field analyzer (RFA). The collector currents measured for two values of the grid bias (0 V and –50 V) are then used to calculate the secondary electron yield as $\delta = [I_C(0\text{ V}) - I_C(-50\text{ V})]/I_0$, where I_0 is the beam current and $I_C(\varphi)$ is the collector current as a function of the retarding potential. Another common procedure is to measure the sample current with and without +50 V bias applied to the sample. For thick samples (no transmission), one then has $\delta = [I_S(50\text{ V}) - I_S(0\text{ V})]/I_0$ with I_S the sample current and its argument the sample bias. (In both cases, the 0 V may be replaced with a small negative voltage to avoid recapture of electrons.) Gineste et al.[10] use a retarding potential generated by negatively biased metal plate in the same plane as the sample and surrounding it. The hemispherical retarding field analyzer has the advantage of better preserving an angle-independent (spherically symmetric) high-pass cutoff energy. This is desirable for best energy resolution by the analyzer. On the other hand, to the extent that electrons collide with the grids, they are a potential source of measurement artifacts. The sample bias methods invert the advantage and disadvantage of the first by dispensing with the grid and collector.

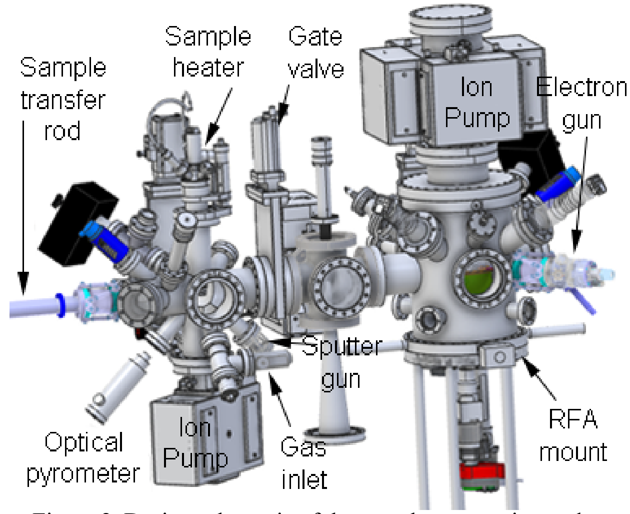

Figure 2. Design schematic of the sample preparation and measurement chambers (left and right of the gate valve).

Since SE are electrons with energies below 50 eV, the IMFP is usually less than 1 nm. This implies that any contamination layer at the surface will critically affect the resulting yield. This sensitivity likely accounts for much of the inter-laboratory variation in measured values. For this reason, our yield measurement system under construction will be housed within an ultra-high vacuum (UHV) system with a sample preparation chamber (left of the gate valve Fig. 2) equipped with facilities for sputtering, low-energy electron bombardment,[11,12] contaminant removal via reactive gas chemistry, and annealing. The measurement chamber is to the right of the gate valve. Each chamber is pumped with an ion pump (shown) and a turbo pump (out of view on the back side in Fig. 2).

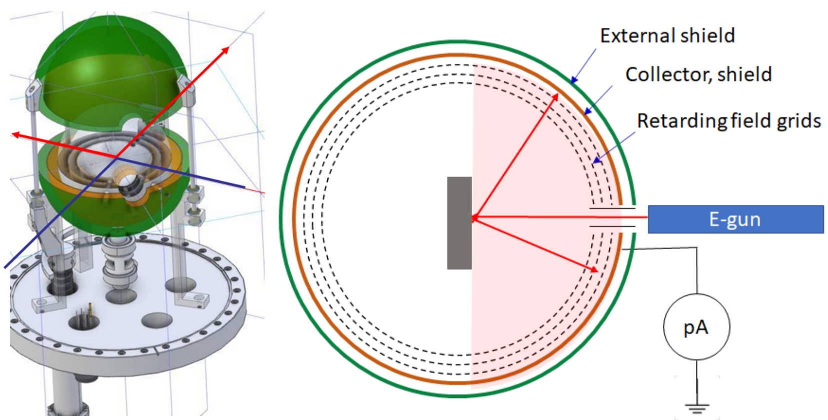

Figure 3. Schematics of the RFA, 3-D rendering (left) and cross section (right)

A spherical retarding field analyzer (Fig. 3) will be inserted into the measurement chamber through the flange on the bottom. The RFA consists of 5 spherical shells. The outermost is a grounded shield to prevent stray external electrons from reaching the interior. Then, in order of decreasing radius, there is a collector, two wire-mesh grids biased –5 kV to 0 V with respect to the sample to create a high-pass filter, then finally a space-charge grid that may be positively biased to draw emitted electrons away from the sample. The outer shells will be made of a high-permeability material to act as magnetic shielding. The grids will be high transparency metal meshes. The system is designed to permit measurement of secondary- and backscattered-electron yields and emission energy spectra. Measurements will be “absolute,” that is, ratios of currents measured with high (and equal) collection efficiency, as opposed to signals converted to grayscale values with poorly known conversion factors or collector efficiency as in an SEM. All signals may be measured as functions of the beam energy and angle of incidence. We chose the spherical design for best energy resolution. Angle of incidence variation will be accomplished by rotating the sample up to 90º. For a normally incident beam, electrons are emitted into the shaded (Fig. 3) hemisphere. Rotation exposes an additional quadrant. The remaining “inactive” quadrant is unseen by electrons. Mounting hardware is concentrated in the inactive quadrant to keep the active ones as uniform as possible, thereby minimizing any change of detector efficiency with angle. The electron beam will be introduced through the shield, collector, and grids via a drift tube. The sample, grids, drift tube, and collector can be independently biased, and picoammeters will measure currents to or from each. We plan to also at least initially use the RFA to acquire Auger electron spectra with which to ascertain the cleanliness of samples when they are transferred from the sample preparation chamber. There is an available port for a dedicated Auger spectrometer if one is needed.

In this way, detailed measurements of energy spectra and yield as a function of angle from well-characterized samples will be available to challenge beam-sample interaction models.

3. MEASUREMENT INTERCOMPARISONS

In the previous section, we described measurements that aim for quantitative measurements of basic model-predictable quantities in the simplest configurations: polished clean samples with no topography and 2π sr detector collection angle. Such measurements are close to the model, far from the measurement application. Our second project is complementary, closer to the application but further from the model. It is based on intercomparison of measurement techniques. To measure, e.g., a linewidth or line height, all techniques require a sample-probe interaction model for which there may be associated model errors. Discrepancies among techniques that interact with different uncorrelated physics may reveal the presence and magnitude of modeling errors. We have earlier performed such inter-comparisons, for example between SEM, atomic force microscopy, and electrical critical dimension (ECD) measurements;[13] SEM and ECD;[14] SEM top-down and SEM cross-section on Si[15] and resist[16] lines; and SEM, scanning transmission electron microscopy (STEM) cross-section, and critical dimension small-angle x-ray scattering (CD-SAXS).[17] In all of these, the lines were patterned on the surface of a wafer.

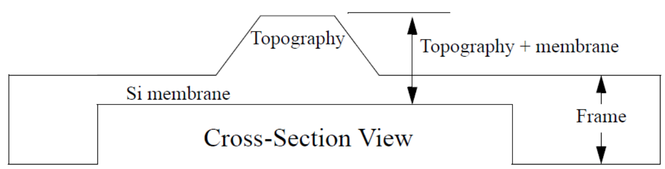

Figure 4. Schematic of a patterned line on a thin membrane

In the current project, we are fabricating line/space arrays on thin (≈200 nm) Si membranes (Fig. 4). Even after etch, the membranes remain thicker (> 100 nm) than the roughly 35 nm range of a critical dimension SEM’s 1 keV (or lower) electrons. These films should be indistinguishable from a full-thickness wafer at these low energies. However, the same lines are measurable in transmission, either in the SEM at 20 keV or 30 keV or in a dedicated STEM at higher energies. Arrays with large enough lateral extent should be measurable by CD-SAXS.

A noisy and uncalibrated preliminary measurement is shown in Fig. 5. Two simultaneously acquired images, one by bright field STEM and one in SE mode, are shown on top. Linescans between the horizontal markers on the image are averaged to produce the signals plotted on the bottom. We should in principle be able to derive topographies (height, width, shape, etc.) for which STEM and SE simulations produce the corresponding signals. Since signals come from the same topography, we expect a match if the models are correct. The STEM signal depends strongly on elastic scattering of high energy electrons whereas the SE signal’s dependence is mainly on generation and transport of low-energy SE. These models employ different physics. Disagreement would challenge existing models.

4. MODEL IMPROVEMENT

SE comprise the main signal in SEM. A key quantity of interest for SE generation is the doubly differential cross section for inelastic events in which the incident electron transfers energy ω and momentum q to a secondary electron. In the first Born Approximation, this is given as[18]

$$\frac{d^2\sigma}{d\omega dq} = \frac{2}{\pi N v^2 q}\mathrm{Im}\left[-\frac{1}{\varepsilon(q,\omega)}\right] \tag{1}$$

with N the number density of scatterers and v the speed of the incident electron.

By integration of this equation over the kinematically allowed range of ω and q, we can obtain the total cross section, σ, and the inverse IMFP, $\lambda^{-1} = N\sigma$. The probability distribution functions for ω and q that are needed to construct a Monte Carlo simulator are obtained with less than full integration. The key requirement, then, is a model for the dielectric function of the medium. Hence, a first step to improving calculations of λ, ω, and q is to improve the model for calculating the dielectric function.

Penn introduced a model dielectric function that made use of the readily available optical data for $\varepsilon(q = 0, \omega)$ for various materials.[19,20] His model extends ε to non-zero q by use of the Lindhard dielectric function, based on the Random Phase Approximation (RPA) from quantum mechanics. This approach gives results that compare reasonably well with experimental data for high energies, but there are discrepancies in the low energy regime relevant for SEM.[2,21,22]

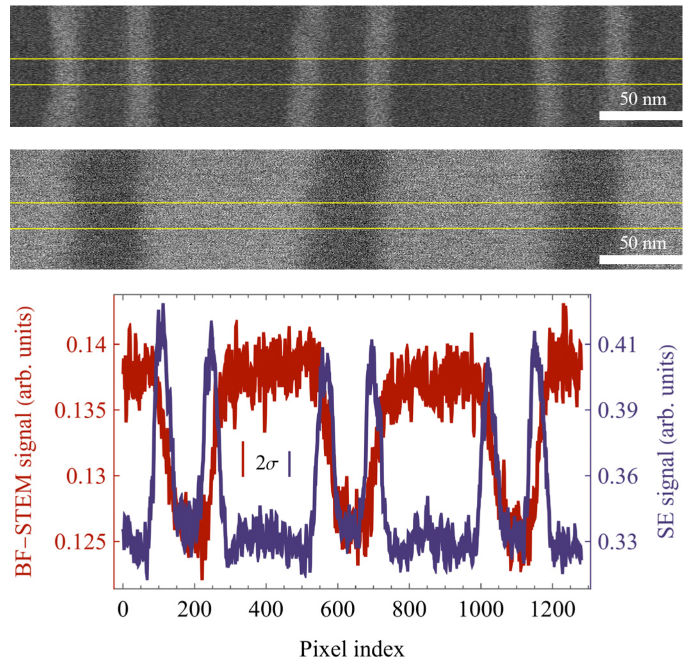

Figure 5. Upper: SE image at 30 keV of a line-space array at approx. 150 nm pitch. Line edges are bright. Middle: Bright-field STEM image acquired simultaneously with the upper image. Lines are dark and spaces bright. Bottom: Regions between the horizontal markers in the images are averaged vertically to produce these representative overlaid linescans. Vertical lines to the left and right of "2σ" are ±σ repeatabilities of STEM and SE curves respectively.

Others have tried to address the limitations of this approach through the introduction of plasmon damping with a Mermin-type dielectric function,[23] inclusion of local field effects,[24,25] and other many-body effects arising from the Coulomb interaction,[26] which the Lindhard/RPA dielectric function does not include, to varying degrees of success. Some inherent limitations of these optical-data models are the dependence on experimental data and the errors associated with them, the lack of data for some materials and some energy ranges, and the theoretical basis for the extrapolation to non-zero q.[2]

One proposed approach is to use an *ab initio* method like ground state Density Functional Theory (DFT) to calculate $\varepsilon(q = 0, \omega)$, and then use it as input to the Penn-type models.[2] Another approach is to use DFT to calculate the dielectric function for all q, and then obtain the differential cross section directly.[27] DFT includes exchange and correlation effects so should be an improvement over Lindhard/Mermin dielectric models that do not, but for some materials like Si where electron-hole excitations are significant, it gives poor results.[28] This isn't too surprising given that ground state DFT does not guarantee a proper treatment of the excitations in materials.[29]

Extensions of DFT-like time dependent density functional theory (TDDFT) attempt to address this and can give results in good comparison to experiments for molecules and smaller structures.[30,31]

TDDFT has been applied to solids like Cu and has been claimed to give better comparison with experiments compared to optical data models,[32,33] but in such a material, even ground-state DFT gives good agreement with the experiments.[27] Electrons in a metal like Cu experience more screening, which makes many-body effects from excitations less significant,[29] so it is unclear what improvements to the IMFP arise from TDDFT alone. One of the main limitations of applications of TDDFT to general solids arise from the lack of good functionals that can capture the nature of excitations in materials like Si.[31,34]

This project aims to implement a calculation of the energy- and momentum-dependent ELF for materials like Si using ground-state DFT as the starting point and solving the Bethe-Salpeter Equation (BSE) for the excitations. The BSE treats excitations systematically and unambiguously and has been successfully applied to a range of systems, from small molecules to solids, with exceptional agreement with experiments.[34-38] For Si, it has been successfully used to calculate highly

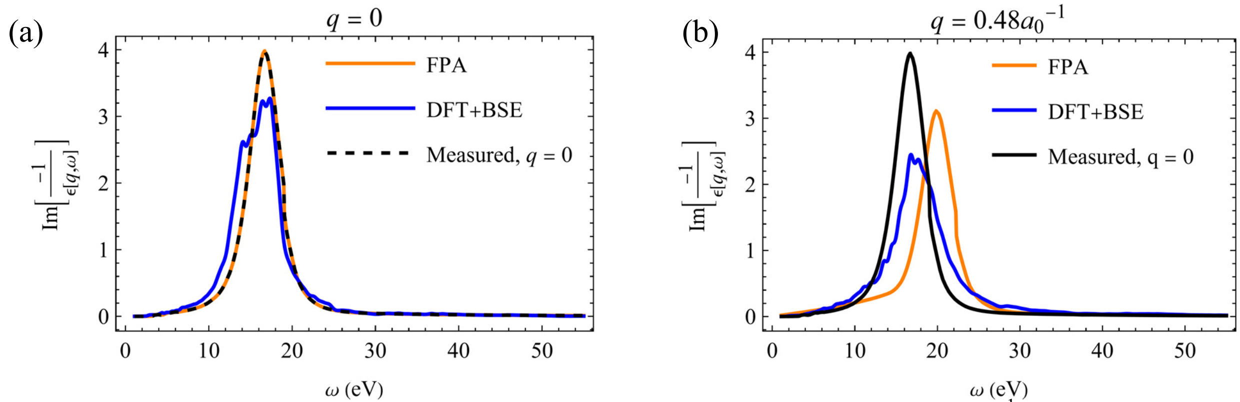

Figure 6. Comparison of the energy loss function at low energy for Si at (a) $q = 0$ and (b) $q = 0.48a_0^{-1}$, a_0 the Bohr radius, as calculated by the FPA and DFT+BSE methods. The measured function at $q = 0$ is shown for reference in both *a* and *b*.

accurate optical ELF in the low energy regime important for SEM. Preliminary results in our initial approximation are shown in Fig. 6, where they are compared to the full Penn algorithm. At $q = 0$ (Fig. 6a), the FPA agrees exactly with the measured energy loss function, as it must by construction. At higher q, the FPA peak shifts to higher energy at a faster rate than does the DFT+BSE result. At $q = 0.48a_0^{-1}$ (Fig. 6b), the FPA peak has shifted approximately 3 eV to the right as required for a free-electron dispersion, but the DFT+BSE calculation shows a smaller energy shift, driven in part by details of the band structure. Future work will include the couplings that can arise between excitons and plasmons, a many-body effect that's been shown to be important in Si.[28,39,40] This approach will then be used to obtain momentum and energy dependent ELFs for subsequent calculation of IMFPs, secondary yields, etc. for Si and other materials of technological interest.

5. SUMMARY

We are undertaking several new projects to validate models of signal generation in the SEM. Two of the projects are focused on testing models with careful measurements. One of these will measure secondary- and backscattered-electron yields (ratios of emitted electrons in each category to incident beam electrons) and energy spectra as functions of electron beam energy and angle of incidence. The detector will be a spherical retarding field analyzer that surrounds the sample completely except for a small entrance aperture for the incoming beam. It will be housed in an ultra-high vacuum chamber with facilities to put the sample into a reproducibly clean state. Such yields are basic quantities predicted by signal models. Another project will compare measurements by different techniques on samples with topography. In this case there are two models in play, one for each of the compared techniques. This makes diagnosis of discrepancies more difficult. The offsetting advantage is that such more complicated samples represent an important intended application of the SEM. This is therefore a more complete test of how the instrument is used in practice. The final project is a theoretical one meant to give us options if (when?) we uncover discrepancies between measurements and predictions.

REFERENCES

[1] *IEEE International Roadmap for Devices and Systems--Metrology* (2022), Available at: https://irds.ieee.org/ (Accessed: February 8, 2023).

[2] D. Emfietzoglou et al., "Inelastic mean free path of low-energy electrons in condensed media: beyond the standard models," Surf. Interface Anal. **49**, 4 (2017) [doi:10.1002/sia.5878].

[3] H. T. Nguyen-Truong, "Low-energy electron inelastic mean free paths for liquid water," J. Phys.: Condens. Matter **30**, 155101 (2018) [doi:10.1088/1361-648X/aab40a].

[4] D. Joy, "A Database on Electron-Solid Interactions," Scanning **17**, 270 (1995).

[5] R. Shimizu, "Secondary electron yield with primary electron beam of kilo-electron-volts," J. Appl. Phys. **45** (1974)

[6] V. Baglin et al., "The Secondary Electron Yield of Technical Materials and its Variation with Surface Treatments," CERN-LHC-Project-Report-433, CERN LHC (2000).

[7] C.G.H. Walker et al., “The secondary electron emission yield for 24 solid elements excited by primary electrons in the range 250-5000 eV: a theory/experiment comparison,” Scanning **30**, 365 (2008) [doi:10.1002/sca.20124]

[8] I. M. Bronstein and B. C. Fraiman, *Secondary Electron Emission*, Nauka, Moscow (1969)

[9] T. Koshikawa and R. Shimizu, “Secondary electron and backscattering measurements for polycrystalline copper with a spherical retarding-field analyser,” J. Phys. D: Appl. Phys. **6**, 1369–1380 (1973) [doi:10.1088/0022-3727/6/11/312].

[10] T. Gineste et al., “A novel experimental setup for the measurement electron backscattering yield,” Meas. Sci. Technol. **25**, 085601 (2014).

[11] E. Materna Mikmeková et al., “Contamination Mitigation Strategy for Ultra-Low Energy Electron Microscopy and Spectroscopy,” Microsc. Microanal. **25**, 500 (2019).

[12] A. Vladár, D. Hoyle, and H. Kotaro, “Electron Irradiation Cleaning of the SEM and its Samples,” Microsc. Microanal. **27**, 434 (2021)

[13] J. S. Villarrubia et al., “Intercomparison of SEM, AFM, and Electrical Linewidths,” Proc. SPIE **3677**, 587-598 (1999) [doi:10.1117/12.350846].

[14] J. S. Villarrubia et al., “Linewidth Measurement Intercomparison on a BESOI Sample,” Proc. SPIE **3998**, pp. 84-95 (2000) [doi:10.1117/12.386488].

[15] J. S. Villarrubia et al., “Scanning electron microscope analog of scatterometry,” Proc. SPIE **4689**, pp. 304-312 (2002) [doi: 10.1117/12.473470].

[16] J. S. Villarrubia et al., “Dimensional Metrology of Resist Lines using a SEM Model-Based Library Approach,” Proc. SPIE **5375**, pp. 199-209 (2004). [doi:10.1117/12.536871].

[17] J. S. Villarrubia et al., “Scanning electron microscope measurement of width and shape of 10nm patterned lines using a JMONSEL-modeled library,” Ultramicroscopy **154**, 15–28 (2015) [doi:10.1016/j.ultramic.2015.01.004].

[18] H. Shinotsuka et al., “Calculations of electron inelastic mean free paths. XII. Data for 42 inorganic compounds over the 50 eV to 200 keV range with the full Penn algorithm,” Surf. Interface. Anal. **51**, 427–457 (2019) [doi:10.1002/sia.6598]

[19] D. R. Penn, “Electron mean free paths for free-electron-like materials,” Phys. Rev. B **13**, 5248–5254 (1976) [doi:10.1103/PhysRevB.13.5248].

[20] D. R. Penn, “Electron mean-free-path calculations using a model dielectric function,” Phys. Rev. B **35**, 482–486 (1987) [doi:10.1103/PhysRevB.35.482].

[21] C. J. Powell and A. Jablonski, “Evaluation of Calculated and Measured Electron Inelastic Mean Free Paths Near Solid Surfaces,” Journal of Physical and Chemical Reference Data **28**, 19–62 (1999) [doi:10.1063/1.556035].

[22] M. Vos and P. L. Grande, “How the choice of model dielectric function affects the calculated observables,” Nuclear Instruments and Methods in Physics Research Section B: Beam Interactions with Materials and Atoms **407**, 97–109 (2017) [doi:10.1016/j.nimb.2017.05.064].

[23] B. Da et al., “Extended Mermin Method for Calculating the Electron Inelastic Mean Free Path,” Phys. Rev. Lett. **113**, 063201 (2014) [doi:10.1103/PhysRevLett.113.063201].

[24] W. Hanke and L. J. Sham, “Local-field and excitonic effects in the optical spectrum of a covalent crystal,” Phys. Rev. B **12**, 4501–4511 (1975) [doi:10.1103/PhysRevB.12.4501].

[25] W. Hanke and L. J. Sham, “Many-particle effects in the optical spectrum of a semiconductor,” Phys. Rev. B **21**, 4656–4673 (1980) [doi:10.1103/PhysRevB.21.4656].

[26] Z. H. Levine and D. C. Allan, “Linear optical response in silicon and germanium including self-energy effects,” Phys. Rev. Lett. **63**, 1719–1722 (1989) [doi:10.1103/PhysRevLett.63.1719].

[27] W. S. M. Werner, K. Glantschnig, and C. Ambrosch-Draxl, “Optical Constants and Inelastic Electron-Scattering Data for 17 Elemental Metals,” Journal of Physical and Chemical Reference Data **38**, 1013–1092 (2009) [doi:10.1063/1.3243762].

[28] V. Olevano and L. Reining, “Excitonic Effects on the Silicon Plasmon Resonance,” Phys. Rev. Lett. **86**, 5962–5965 (2001) [doi:10.1103/PhysRevLett.86.5962].

[29] K. Capelle, “A bird’s-eye view of density-functional theory,” Braz. J. Phys. **36**, 1318–1343 (2006) [doi:10.1590/S0103-97332006000700035].

[30] E. Runge and E. K. U. Gross, “Density-Functional Theory for Time-Dependent Systems,” Phys. Rev. Lett. **52**, 997–1000 (1984) [doi:10.1103/PhysRevLett.52.997].

[31] R. J. Magyar and S. Tretiak, "Dependence of Spurious Charge-Transfer Excited States on Orbital Exchange in TDDFT: Large Molecules and Clusters," J. Chem. Theory Comput. **3**, 976–987 (2007) [doi:10.1021/ct600282k].
[32] M. P. Polak and D. Morgan, "MAST-SEY: MAterial Simulation Toolkit for Secondary Electron Yield. A monte carlo approach to secondary electron emission based on complex dielectric functions," Computational Materials Science **193**, 110281 (2021) [doi:10.1016/j.commatsci.2021.110281].
[33] H. T. Nguyen-Truong, "Electron inelastic mean free path at energies below 100 eV," J. Phys.: Condens. Matter **29**, 215501 (2017) [doi:10.1088/1361-648X/aa6b9d].
[34] G. Onida, L. Reining, and A. Rubio, "Electronic excitations: density-functional versus many-body Green's-function approaches," Rev. Mod. Phys. **74**(2), 601–659 (2002) [doi:10.1103/RevModPhys.74.601].
[35] S. Albrecht, G. Onida, and L. Reining, "Ab initio calculation of the quasiparticle spectrum and excitonic effects in Li 2 O," Phys. Rev. B **55**, 10278–10281 (1997) [doi:10.1103/PhysRevB.55.10278].
[36] L. X. Benedict, E. L. Shirley, and R. B. Bohn, "Optical Absorption of Insulators and the Electron-Hole Interaction: An *Ab Initio* Calculation," Phys. Rev. Lett. **80**, 4514–4517 (1998) [doi:10.1103/PhysRevLett.80.4514].
[37] M. Rohlfing and S. G. Louie, "Excitonic Effects and the Optical Absorption Spectrum of Hydrogenated Si Clusters," Phys. Rev. Lett. **80**, 3320–3323 (1998) [doi:10.1103/PhysRevLett.80.3320].
[38] J. A. Soininen and E. L. Shirley, "Scheme to calculate core hole–electron interactions in solids," Phys. Rev. B **64**, 165112 (2001) [doi:10.1103/PhysRevB.64.165112].
[39] T. Sander, E. Maggio, and G. Kresse, "Beyond the Tamm-Dancoff approximation for extended systems using exact diagonalization," Phys. Rev. B **92**, 045209 (2015) [doi:10.1103/PhysRevB.92.045209].
[40] M. Grüning, A. Marini, and X. Gonze, "Exciton-Plasmon States in Nanoscale Materials: Breakdown of the Tamm-Dancoff Approximation," Nano Lett. **9**, 2820–2824 (2009) [doi:10.1021/nl803717g].